Yaw control of a hovering flapping-wing aerial vehicle with a passive wing hinge

Yogesh Chukewad[1] and Sawyer Fuller[2]

***Abstract*—Flapping-wing insect-scale robots (<500 mg) rely on small changes in drive signals supplied to actuators to generate angular torques. Previous results on vehicles with passive wing hinges have demonstrated roll, pitch, and position control, but they have not yet been able to control their yaw (heading) angle while hovering. To actuate yaw, the speed of the downstroke can be changed relative to the upstroke by adding a second harmonic signal at double the fundamental flapping frequency. Previous work has shown that pitching dynamics of a passive spring-like wing hinge reduces the aerodynamic drag available to produce yaw torque. We introduce three innovations that increase yaw actuation torque: 1) a new two-actuator robot fly design that increases the moment arm, 2) wider actuators that increase the operating frequency, and 3) a phase shift to the second harmonic signal. We validated these results through simulation and experiment. Further, we present the first demonstration of yaw angle control on a passive-hinge vehicle in a controlled flight. Our new robot fly design, UW Robofly-Expanded, weighs 160 mg (two toothpicks) and requires only two piezo actuators to steer itself.**

***Index Terms*—Micro/Nano Robots, Aerial Systems: Mechanics and Control, Biologically-Inspired Robots**

I. Introduction

INSECT-SCALE flying robots (<500 mg) have the potential for several applications such as search and rescue, surveillance, and environmental monitoring, due to their small size and large deployment numbers. First feedback-controlled hovering of an insect-robot, RoboBee, was demonstrated in [1], in which all but the yaw degree of freedom were controlled. Another design, Robofly, at the similar size was introduced in the authors' earlier work in [2], [3], [4].

Despite recent developments in sensing, power, and control, we are yet to see an insect-sized dual-actuator robot with controlled heading or yaw angle (see Fig. 1 for yaw axis) while hovering. As mentioned in [6], control of the yaw angle of the robot is desirable for many reasons including, 1) legs required to be in specific orientation for landing, 2) sensor (for example, camera and IR sensor) required to point in a particular direction, or 3) to reduce computation complexity of the controller (a computationally intensive switching between global and body coordinate frames for lateral position control can be reduced or completely eliminated).

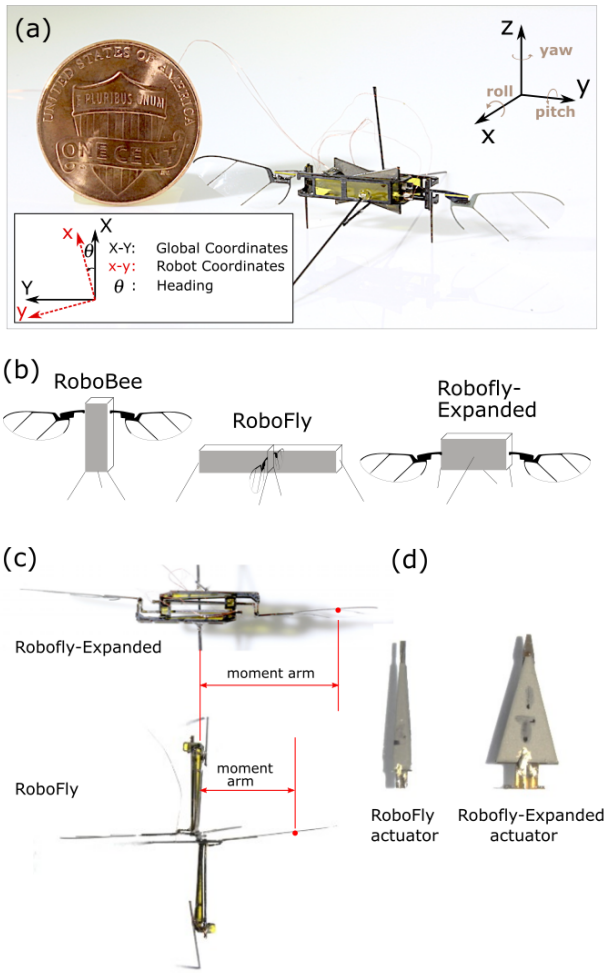

Fig. 1. (a) Robofly-Expanded, a new design of a robot fly [5]. A U.S. penny is shown for scale. Inset shows how heading (absolute yaw angle) θ is measured between world and robot coordinate systems, about the positive world Z-axis. (b) Comparison of Robofly-Expanded with earlier versions of flapping-wing robots: RoboBee [1] and RoboFly [2]. (c) Comparison of the moment arm (distance from the center of mass to the center of pressure) of Robofly-Expanded with that of RoboFly. (d) Comparison of the width of actuators of RoboFly and Robofly-Expanded.

The challenge of yaw actuation in passive-hinge vehicles is not new. Flapping with a passive hinge represents a distinct class of aerodynamic system with behavior that differs from systems in which wing motion is entirely specified [7]. Yaw torque measurements in the two-actuator Harvard Robobee affixed to a capacitive torque sensor suggested the ability

Manuscript received: August, 16, 2020; Revised December, 22, 2020; Accepted January, 28, 2021.

This paper was recommended for publication by Editor Xinyu Liu upon evaluation of the Associate Editor and Reviewers' comments. This work was partially supported by the Air Force Office of Scientific Research under grant no. FA9550-14-1-0398. *(Corresponding Author: Yogesh Chukewad)*

[1]Yogesh Chukewad is with Unchained Labs, 6870 Koll Center Pkwy, Pleasanton, CA 94566, USA. [2]Sawyer Fuller is with the Department of Mechanical Engineering, University of Washington, Seattle, WA 98195, USA yogeshc@uw.edu, minster@uw.edu

Digital Object Identifier (DOI): see top of this page.

to produce significant yaw torque [8]. The technique relied on its piezo actuator's ability for high-bandwidth actuation, by flapping the wing in one direction faster than the other direction. Air drag varies approximately with velocity squared in the inertia-dominated fluid mechanics of this scale (Re ≈3000 [9]), so that the net stroke-averaged drag force can be varied. But in videos of its first controlled flights it can be observed that yaw angle rotated freely [1]. Indeed, significant efforts needed to be undertaken in that work to design a nonlinear controller that could operate regardless of orientation. For this reason it is likely that the previously - measured yaw torques could be attributable to sensing error.

At insect scale, the most successful previous demonstration is hovering control of the yaw came in a design with two extra actuators [10], for a total of four. A sophisticated linkage allowed this robot to vary the wing hinge, to actuate the angle of attack (AoA) to actuate yaw [11]. Like flies, this robot used a passive wing hinge whose neutral angle was under active control [12].

Successful yaw actuation on minimally-actuated (one actuator per wing) have included a Robobee steered left and right using rapid, phased pitch and roll oscillations, exploiting the nonlinearity of attitude kinematics [6]. This expends significant energy, was hard to control, and was not able to consistently steer in a desired direction. In [13], a four-winged robot actuated yaw in free flight by extending the moment arm, but controlled flights in which yaw was controlled yaw were not demonstrated.

Yaw torque in passively-pitching wings with a spring-like restoring moment was more closely investigated in [14]. That work revealed that due to the wing hinge and to the effect of taking the time-integral of drag force on the wing, the yaw torque could reverse sign. The magnitude of this "torque inversion" peaks at the peak lift-to-drag ratio. That work proposed additional features that established a nonlinear stress curve for the wing hinge, negating the torque inversion.

Due to this challenge, no demonstration of yaw control on a minimal (two-actuator) vehicle with spring-like hinges has been made. It is not known whether wings with a physical limit to the angle of attack are more efficient than spring-like hinges, but the latter are likely to be quieter and may avoid fatigue-based failure. Steinmeyer [15] showed that yaw can be actuated successfully on a tethered flapper equipped with simple linear spring hinges if the robot is driven below its resonant frequency. At lower frequencies, the torque inversion regime can be avoided. But no controlled flight demonstrations have been reported to date. For controlled flight, cross-coupling between modes of actuation can either be neglected or modelled, both of which have associated challenges. In particular, the weaker the yaw actuation authority, the stronger the signal must be to attain consistent control over that degree of freedom. Anecdotal evidence suggests that the complicated motions of flapping-wing flight have cross-coupled interactions, which are exacerbated as the actuation signal increases. But in free-flight, a yaw controller must not disrupt other actuation modes. We conjecture that the foregoing challenges have precluded free-flight yaw control until now.

To address the problems mentioned in earlier research on yaw control, we introduce and validate two key innovations that are designed to increase yaw authority on vehicles with spring-like passive wing hinges. First, we show that a new robot fly design, that reorients its piezo actuators laterally (Fig. 1(b)) and moves its wings farther from the center of mass to increase moment arm (Fig. 1(c)), is able to increase its yaw actuation authority. Called Robofly-Expanded (Fig 1) [5], we demonstrate that through this change it is able to actuate and control its yaw angle while hovering using PD control. The robot is able to follow simple trajectories while hovering. Second, we show that by changing the phase of the higher frequency excitation of the wings, even greater yaw torque is possible. We validate these results using quasi-steady analytical model for the flapping wing, as well as a lumped-parameter model of the actuator-wing system.

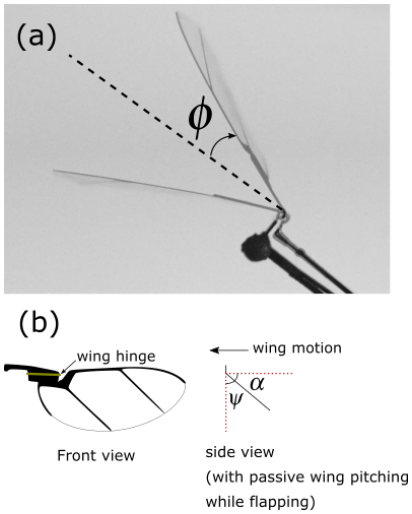

Fig. 2. (a) Wing angle $\phi(t)$, measured using frames from high-speed video. The wing is flapped at 190 Hz, providing ≈10 frames per stroke. (b) A drawing of a wing in frontal view; its passive wing hinge can be seen. On the right is a side view (along the length of the wing) showing the passive wing pitching angle while flapping. The angle of attack, α, is measured relative to the horizontal plane, whereas wing hinge angle, ψ, is measured relative to the vertical plane.

TABLE I
PARAMETERS AND THEIR VALUES USED FOR IN SIMULATIONS

Parameter	Symbol	Value
Density of air	ρ	1.23 $kg\ m^{-3}$
Distance from CM to CP	r_{cp}	2.03 cm
Distance from wing base to midpoint of the wing along its length	r_{b-w}	9.0 mm
Peak-to-peak wing amplitude	Φ	54°
Flapping frequency	$\frac{\omega}{2\pi}$	190 Hz
Wing hinge parameter	β	10.32 $ms^{-1}rad^{-1/2}$
Wing mass	m	0.63 mg
Stiffness of combined actuator and transmission	K_{act}	105 $\mu Nmrad^{-1}$
Vertical distance from wing center of pressure to hinge	z_{cp}	1.25 mm
Hinge stiffness	k	4.4 $\mu Nmrad^{-1}$
Wing area	A	51.2×10^{-6} m^2

This article has been accepted for publication in a future issue of this journal, but has not been fully edited. Content may change prior to final publication. Citation information: DOI 10.1109/LRA.2021.3060726, IEEE Robotics and Automation Letters

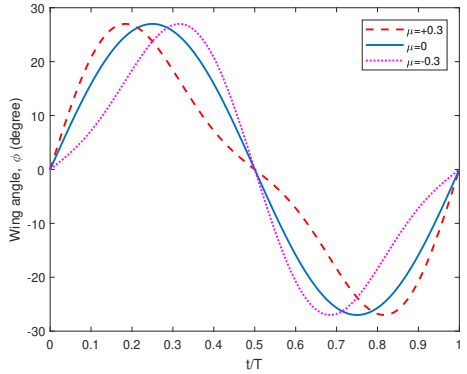

Fig. 3. Wing angle $\phi(t)$, normalized by flapping time period, for three different values of the second harmonic factor μ. The wing angle ϕ is scaled so that the peak magnitude achieved in a given cycle is the same regardless of μ value.

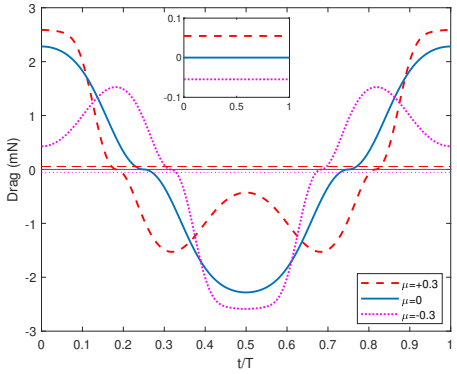

Fig. 5. Simulation results of drag acting on a flapping wing changing with time (normalized by flapping time period), for three different values of μ. Non-zero values of μ show differential-drag generation. Horizontal lines on the main plot (also magnified in the inset) show the stroke-averaged drag values for corresponding values of μ.

II. Yaw Torque Generation

A. Robot Design

As introduced in [5], the robot has its actuators re-oriented so that their long axes are horizontal and along the body pitch axis (Fig. 1). One of the desirable effects of moving the wings father apart from the center of mass (CM) of the body is a larger moment arm. The larger moment arm, coupled with drag induced by the flapping wings, leads to larger yaw torque generation.

The robot is also equipped with wider actuators (Fig. 1(d)) which, in combination with the transmission, leads to a higher resonant flapping frequency of $\approx$ 200 Hz. A drawing of the wing and its passive wing hinge is shown in Fig. 2. Its wing hinges are passive spring-like flexure joints made of thin Kapton that produce passive pitching while flapping. They are $3\times$ stiffer than those of Robofly [2] and Robobee [16] to match the $3\times$ wider actuators. The effect of passive wing rotation is studied in detail and related equations of motion are derived in [17], [18]. The new design of actuators along with stiffer wing hinges allows the robot to lift more payload. For better yaw control authority, these robots are always flown with a lower payload than the maximum it can lift. This allows the robot to operate at off-optimal conditions, in which it produces significantly lower (yet larger than its own weight) lift than it can. The effect of the off-optimal conditions is explained in detail in the following subsection.

B. Torque generation

The only actuation mode that has produced measurable yaw torques consists of creating differential drag on wings by flapping them faster in one direction than the other. One of the ways to generate such split-cycle modulation is by actuating with voltage signal which also includes the second-harmonic frequency [1]. When the actuators are supplied with this voltage signal, the wing flapping angle, $\phi(t)$ is written as follows.

$$\phi(t) = \frac{\Phi}{2}\frac{\sin(\omega t) + \mu\sin(2\omega t)}{\max[\sin(\omega t) + \mu\sin(2\omega t)]} \tag{1}$$

Here, ω is the wing angular velocity in rad/s, Φ is the peak-to-peak wing amplitude, and μ is the peak-to-peak amplitude of the second harmonic term, relative to the fundamental frequency term. The term μ is referred to as the second harmonic factor in the rest of the paper. The variation of wing angle while flapping is shown in Fig. 3 for $\mu = 0$ and for its extreme values of $+0.3$ and -0.3. We carried out experiments and observed that the total amplitude was the same for any value of μ, provided other parameters were kept constant. Therefore, we used the normalizing term in Eq. 1 to match the peak-to-peak amplitude for any value of μ in the simulation.

We present a model, inspired by [14], that entails purely-translational wing motion and a quasi-steady aerodynamic model to predict yaw torque behavior. The quasi-steady model incorporates unsteady flow effects in flapping wings such as the leading edge vortex into effective lift and drag coefficients [19], [20]. To simplify the simulation, we assume that wing rotation about its passive hinge is a direct function of wing flapping velocity, assuming that inertial dynamics around the wing hinge are fast relative to flapping frequency.

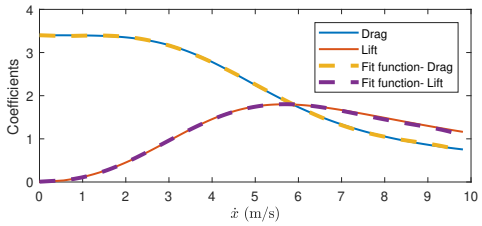

Fig. 4. Model for C_{drag} and C_{lift} vs wing velocity $\dot{x}$ (translational velocity of the midpoint of the wing along its length) for Robofly wing hinge. Dashed lines indicate polynomial approximation used in simulation.

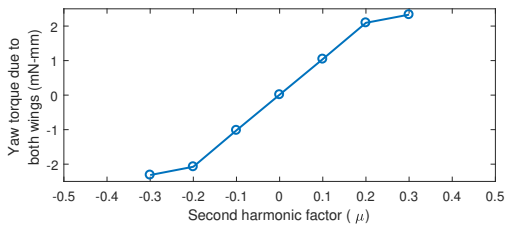

Fig. 6. The variation of stroke-averaged yaw torque generated due to both wings with varying μ, according to the quasi-steady simulation.

Drag acting on the wing, F_{drag}, is given by [18]

$$F_{drag} = \frac{1}{2}\rho C_{drag}(\alpha) A r_{b-w}^2 \dot{\phi} \mid \dot{\phi} \mid \tag{2}$$

where A is wing area and ρ is air density. For simplicity, the quantity r_{b-w} is the distance from the wing base to the midpoint of the wing along its length, C_{drag} is the drag coefficient, which varies as a function of angle of attack (AoA) α [17], [18], [19] given by

$$C_{drag}(\alpha) = 1.9 - 1.5\cos(2\alpha) \tag{3}$$

Similarly, the lift force, F_{lift} is given by [18]

$$F_{lift} = \frac{1}{2}\rho C_{lift}(\alpha) A r_{b-w}^2 \dot{\phi}^2, \tag{4}$$

where C_{lift} is the lift coefficient, a function of α [17], [18], [19], which is given by

$$C_{lift}(\alpha) = 1.8\sin(2\alpha). \tag{5}$$

C_{drag} and C_{lift} are functions of α. For simplicity, we model the system as a linearly translating wing, with position $x = r_{b-w}\phi$. If the α-axis dynamics are assumed to be instantaneous, then steady-state wing velocity is a function of α [14]:

$$\dot{x}_{ss} = \beta\sqrt{\frac{(\pi/2-\alpha)}{\sin(\pi/2-\alpha)C_{lift}(\alpha) + \cos(\pi/2-\alpha)C_{drag}(\alpha)}}, \tag{6}$$

where β is the wing hinge parameter given by $\sqrt{\frac{2k_0}{\rho A z_{cp}}}$.

We performed a simple system identification procedure to determine the value of β. For this purpose, we flapped a wing with a bias signal of 250 V, a sinusoidal signal with a peak-to-peak amplitude $2V_0$ of 140 V to the middle layer (carbon fiber), and at 200 Hz. The wing amplitude, ϕ, and AoA, α, were measured by recording the flapping of the wing using a high-speed camera (Phantom v7.3, Vision Research, Inc.) at 3900 frames per second. Frames at extreme positions of the flapping were captured to measure the peak-to-peak amplitude Φ. Fig. 2 shows an overlay of two frames in which the wing is at the extreme positions while flapping. With the measured amplitude, the wing angle was generated as a sinusoidal function of time. Wing velocity as a function of time was then calculated by taking the time derivative of the wing angle. This function was used to estimate the wing velocity, $\dot{x}_{ss}$ at mid-stroke ($\phi \approx 0$). We also estimated the corresponding α value by measuring the length of the projection of the wing chord in the overhead view. By substituting the values of $\dot{x}_{ss}$ and α in Eq. 6, we determined the value of β, which is specific to the Robofly wing hinge (Table I).

We then substituted the value of β in Eq. 6 and plotted the steady state velocity as a function of α, for a possible range of velocities. We combined the steady-state velocity as the function of α with Eq. 3 and Eq. 5 and determined C_{lift} and C_{drag} as functions of the stead-state velocity. For this simulation we didn't consider the wing inertia and assumed $\dot{x} = \dot{x}_{ss}$. This assumption is consistent with the simplified translational quasi-steady model presented in [14]. We plotted the coefficients as the functions of $\dot{x}_{ss}$ in Fig. 4 along with the polynomial fit functions generated using Curve Fitting Toolbox in MATLAB.

Now, we move on to the simulation part which makes use of the empirical value of the wing hinge parameter. In this part, we decided to simulate for the flapping frequency of 190 Hz to slow down the dynamics in the corresponding experiments which are presented later. Using Eq. 4 and $C_{lift}(\dot{x})$, the required peak-to-peak wing amplitude (Φ) was determined such that the total lift was equal to the weight of the robot.

Referring to the wing angle plotted in Fig. 3 for three different values of μ, the drag was calculated using Eq. 2 and $C_{drag}(\dot{x})$ for one whole cycle and plotted against time in Fig. 5. For $\mu = 0$, it can be seen that the drag force is symmetric about mean stroke position. However, in case of $\mu = 0.3$, the drag is significantly larger in one direction that the other. Similar but opposite pattern was observed in case of $\mu = -0.3$, as expected. The torque due to two wings was then calculated using $\tau_{yaw} = 2r_{cp}F_{drag}$, where r_{cp} is the distance between the CM of the robot and the CP of the wing, projected on horizontal plane. τ_{yaw} is plotted for various values of μ in Fig. 6. The torque values estimated from the simulation are comparable with those from the results presented in [14]. It should also be noted that the torque estimated in our study was during a hovering flight (simulated) while holding a constant altitude i.e. the lift was also sufficient to support the weight of the robot. Although our robot is able to generate a large amount of yaw torque as well as lift in the simulation and confirms no anomaly at the operating conditions, it is important to back the results using experiments. The analytical model presented in the work is simple translational quasi-steady, and it doesn't consider wing inertia in the wing pitching dynamics. Our model considers C_{drag} and C_{lift} as functions of wing velocity, and therefore it is more accurate than the models with constant drag and lift coefficients. However, it must be noted that these coefficients are calculated at every step considering that the wing velocity is under the steady state, ignoring the wing inertia. Additionally, actuator dynamics are also not considered in the model. However, we believe that the attenuation of the second harmonic frequency observed by [15] due to actuator dynamics can be addressed by increasing the amplitude of the second harmonic frequency beyond $0.3V_0$. For simplicity, the model considers the translational velocity of the wing at its midpoint along the length while determining the lift and drag forces. A detailed modeling of a similar robot design can be referred to in [14], [15]. To address the limitations of the model in the paper and to ensure that enough amount of yaw torque is generated along with the required lift, demonstrations in hovering experiments are important.

III. Further Increasing Yaw Torque by Adjusting Phase of the Second Harmonic

We have identified an additional mechanism by which to improve yaw torque. The basic principle is to compensate for any phase shift in the second harmonic as it passes through the wing-actuator drive system. If the system is driven slightly below the peak lift to drag ratio [15] to insure that there is

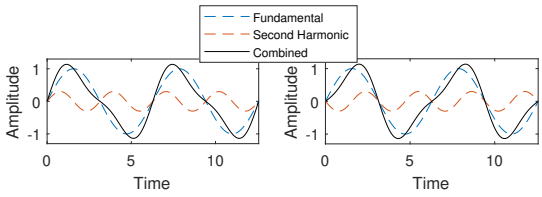

Fig. 7. Sample drive signals given to the actuators for commanding yaw. The combined signal is the sum of the fundamental harmonic and second harmonic signals.

no torque inversion [14], our results indicate that torque can be improved by adjusting the phase of the second harmonic frequency. The behavior of the actuator-transmission-wing system is well approximated by a second-order simple harmonic oscillator [21]. Frequencies higher than the resonant mode, such as the second harmonic, are strongly attenuated [15]. Of particular relevance in the current section is the observation that high frequencies are *also* delayed in phase, which, to our knowledge, has not previously been explored in detail. We note at the outset that phase plays an important role in yaw torque. A phase shift of 180° can reverse its direction, as shown in Fig. 7 (left). From the combined signal it can be seen that the wing would flap harder in one direction than the other. However, when a phase delay of 180° is introduced in the second harmonic signal (see Fig. 7 right), the opposite effect is observed. If the downstroke is faster than the upstroke in the first case, the second would lead to the upstroke being faster than the downstroke, in the absence of any phase difference in the system response. Now, assuming we supply the combined signal shown in Fig. 7 (left) to the actuator, and the actuator-wing system introduces a phase difference between its response to the fundamental frequency and the second harmonic frequency, this can lead to a reduced yaw effect and, in some cases, torque in the opposite direction.

To understand how varying phase plays out in practice subject to the filtering effect of the resonant system, we created a simulation and tested the idea on a physical robot. The simulation combined the aerodynamics of linear translation of a wing on a passive hinge (Equations (2–6)) with a second-order lumped-parameter model of the dynamics of the actuator-wing system. The state of the simulation evolves according to

$$\dot{\psi} = \lambda(F_{\perp}(\psi, \dot{x})z_{cp} - k\psi) \quad (7)$$

$$\ddot{x} = \frac{1}{m}(F_{act} - k_{act}x + F_{drag}(\psi, \dot{x})) \quad (8)$$

where $F_{\perp} = F_{lift}\sin\psi + F_{drag}\cos\psi$ is perpendicular component of the aerodynamic total force acting on the wing and F_{act} is the force by the piezoelectric actuator acting on the translating wing, $k_{act} = K_{act}/r_{b-w}^2$ is the effective spring-like restoring stiffness of the system as seen at the point r_{b-w} away from the stroke rotation axis, and m is the mass of the wing. The value λ must take on a large value to drive the dynamics of ψ to quickly satisfy Eq. 6 as $\dot{x}$ changes. It was chosen so that the bandwidth of the ψ dynamics (=λk) is 3000 Hz.

This system was simulated using fixed-step numerical integration to estimate resulting x trajectories under conditions of zero and non-zero second harmonic contributions, driven by

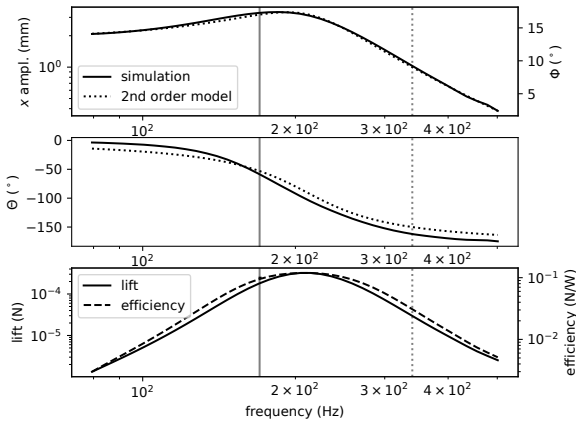

Fig. 8. The frequency response of the simulated system (Eq. (8) resembles a second-order simple harmonic oscillator. (bottom row) The system was driven at 170 Hz (grey vertical line), near its peak efficiency and thrust; the second harmonic frequency is shown as a dashed line. The second harmonic is attenuated (causing $\mu << \mu'$) and has a phase lag. Efficiency = $\int F_{lift}dt / \int |F_{act}\dot{x}|dt$ over a complete cycle.

the function $F_{act} = f_0(\sin(\omega t) + \mu'\sin(2\omega t + \Theta))$, where ω is slightly below the resonant frequency, but still near optimal efficiency (Fig. 8). Fig. 9 shows that by adding positive phase to the second harmonic signal, yaw torque can be increased dramatically, by 36%.

To experimentally validate these results, we suspended the physical robot with a thin Kevlar thread and supplied a drive voltage with smaller amplitude than what is required for lift-off, while varying phase and second harmonic magnitude. The thin thread allowed the robot to spin freely about its yaw axis. We used the MoCap system to measure the maximum yaw velocity achieved after wing flapping started, which is an approximate and convenient way to measure relative yaw torque. The voltage signal supplied to the actuator, which is approximately proportional to actuator force, was $V = V_0\,[\sin(\omega t) + \mu'\sin(2\omega t + \Theta)]$. Fig. 10 shows the resulting yaw velocities at steady-state. Note that the robot was not calibrated to have zero initial yaw torque; instead we show normalized yaw effect relative to that at $\mu' = 0$. The robot shows a stronger yaw torque at non-zero values of Θ, increasing with positive, which is consistent with the predictions of the simulation (Fig. 9). Similarly, a harmonic oscillator driven by a second harmonic above the resonant frequency would show phase lag; addition of phase lead would recover the ideal waveform shown in Fig. 3.

IV. YAW CONTROLLER

We explained the hovering controller of the robot in detail in our earlier work on Robofly [3]. We combined the new yaw controller that works in parallel with the existing hovering controller, as shown in Fig. 12. The robot receives three inputs from the user, which include 1) altitude trajectory, 2) lateral position trajectory, and 3) heading trajectory.

The altitude trajectory is fed into the altitude controller which sends out thrust signals to the robot. The thrust is varied by changing the amplitude of sinusoidal signals supplied to actuators. The lateral controller which is cascaded with

This article has been accepted for publication in a future issue of this journal, but has not been fully edited. Content may change prior to final publication. Citation information: DOI 10.1109/LRA.2021.3060726, IEEE Robotics and Automation Letters

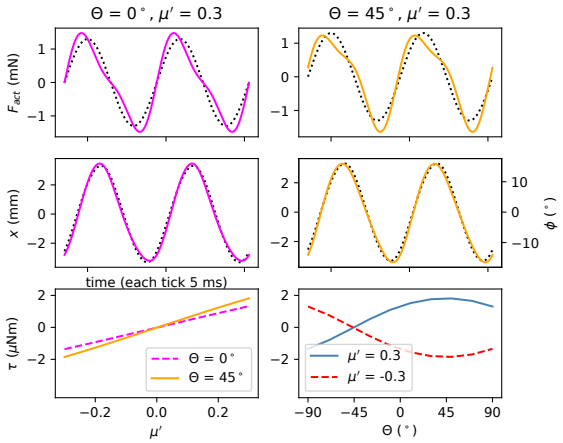

Fig. 9. Simulation indicates that stronger torque can be produced by a second harmonic with a phase lead. (top row) Input actuator forces acting on the translating wing model at 170 Hz. Baseline signal (dotted) vs. with second harmonic (solid). On the left is no phase shift, the right shows a phase shift of 45°. (middle row) The output response of wing-actuator resonant system, which attenuates and phase-shifts the second harmonic signal. The right side shows that adding phase lead produces a more ideal wing motion with a faster upstroke and slower downstroke. (bottom row) Phase lead increases stroke-averaged yaw torque (compare to Fig. 10)

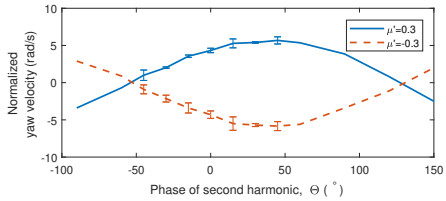

Fig. 10. Experimental results show that adding phase lead Θ to the second harmonic can increase yaw torque, peaking at ≈45°. In these experiments, the robot was hung by a thread and allowed to spin freely under the effect of a yaw command; data points show steady-state yaw velocity, minus the yaw velocity at $\mu' = 0$. Flapping frequency was 170 Hz, V_0=35. For values closer to $\Theta = 0$, three readings were taken, and the median was plotted along with error bar with length equal to the difference between the maximum and the minimum of the three values.

the attitude controller receives the lateral trajectory as the input. The combination of the lateral and attitude controllers determines the roll and pitch torques given to the robot. The yaw controller developed in the current study is then added in parallel with these controllers.

The yaw controller receives the heading trajectory as the input and determines the second harmonic factor, μ', for sinusoidal signals that are supplied to actuators. The voltage signal supplied to the actuator is $V = V_0\,[\sin(\omega t) + \mu' \sin(2\omega t)]$. All of these controllers receive feedback from a motion capture (MoCap) system (four Prime 13 cameras, OptiTrak, Inc., Salem, OR) for robot positions and orientations. This MoCap system sends the data over Ethernet at 240 Hz to the host computer running Simulink Real-Time. The data is sent further over to a xPC Target PC which runs the controller.

The heading, $\theta_d(t)$, is measured between global X-axis and robot's body x-axis (Fig. 1) and about global Z-axis. The feedback to the controller is the actual heading position, $\theta(t)$. The error, $e_\theta(t) = \theta_d(t) - \theta(t)$ is fed into a PD controller. The gains of the PD controller are hand-tuned to achieve the best performance. The control law is given by–

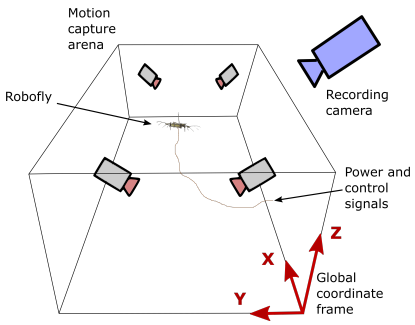

Fig. 11. Motion capture arena. Global coordinate frame is shown for reference. Position of recording camera is shown for better understanding of the view in supplementary video and its frames. The absolute yaw angle (heading) of the robot is measured between body x axis and global X axis, about global Z-axis.

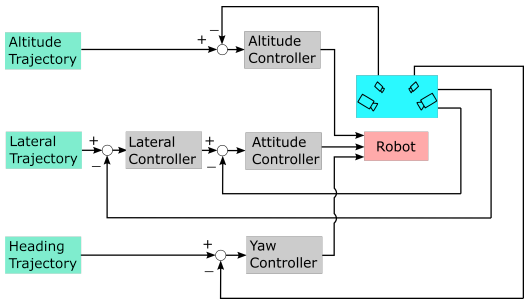

Fig. 12. Controller used for heading control while hovering. The yaw (absolute heading) controller works in parallel with the hovering controller, which consists of an altitude controller and cascaded lateral and attitude controllers. The hovering controller is explained in detail in [3].

$$\mu' = k_{p\theta}\; e_\theta(t) + k_{d\theta}\; \dot{e}_\theta(t) \tag{9}$$

where $k_{p\theta}$ and $k_{d\theta}$ are the proportional and derivative gains, respectively. θ values received from MoCap are first filtered using a low-pass Butterworth filter (cutoff frequency of 240 Hz) before taking derivatives. The output yaw commands are bounded between -0.3 to $+0.3$.

V. Experiments

In this section we demonstrate three sets of results in which the robot follows a desired heading trajectory. In the first experiment, the desired set-point for the heading was held constant, while starting from a random initial heading. In the second experiment, we demonstrated the ability of the robot to steer in both directions. A set-point which changes quickly with time in both directions was given to the robot controller. In the third experiment, we demonstrated the ability of the robot to follow a heading trajectory. All of these experiments were performed on a hovering robot. The flights were recorded using a high-speed camera from the location shown in Fig. 11. These experiments were carried out in the presence of external disturbances coming from equipment with fans nearby. A significant source of perturbation was the set of wire tethers attached to the robot for power signals. The yaw controller had to overcome these disturbances and perturbations to follow the desired heading angle trajectory closely.

As explained in the previous section, we used μ' as the yaw command for controlling the heading of the robot in the

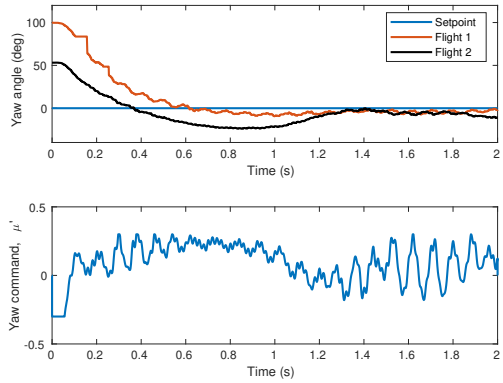

Fig. 13. (Top) Step response of the yaw angle for two independent flights with different initial heading. The robot approaches the setpoint with a very small steady state error. (Bottom) Yaw command corresponding to flight-2 shows a strong control authority as the commands stays within the upper and lower bounds of $+0.3$ and -0.3, respectively.

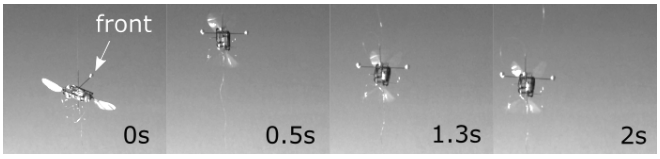

Fig. 14. Frames from a video in which the robot approaches and maintains a constant heading of 0, which corresponds to a vector along the X-axis of the global coordinate frame.

experiments. We found that it was enough to use the second harmonic term in the voltage signal and the robot's widened design presented in this paper to achieve the desired results.

A. Constant set-point

Fig. 13 (top) represents the heading trajectory from two different flight experiments. The robot started from random values of initial headings. The first flight showed little overshoot and faster settling time; however, larger overshoot and longer settling time were observed in the second flight. This can be attributed to disturbances, including the wire tether and wind. The robot approached and stayed at the set-point in both the flights after steady-states were achieved. The RMS errors for the last 0.7 sec in flight-1 and flight-2 are $4.46°$ and $6.47°$, respectively. Yaw commands provided by the controller to actuators for the second flight are plotted in Fig. 13 (bottom). Frames from the second flight are shown in Fig. 14. Front of the robot is shown with an arrow in the first frame, and it can be observed in subsequent frames that the robot heading was at $0°$.

B. Control authority in both directions

Although flight-2 in Fig. 13 (top) showed the ability of the robot to go back to the set-point after an overshoot, we carried out more experiments to demonstrate the control authority in both directions and the ability to react quickly to sharp changes in set-points in any direction. In this experiment, the robot followed a set-point that changed quickly (time period of 1 second) between +60° and 0°. Fig. 15 (top) shows the yaw angle response along with the given set-point in one of the

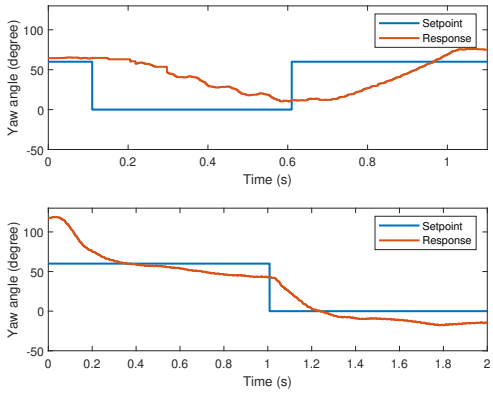

Fig. 15. (Top) Yaw angle (degree) response in a flight in which the set-point is changed mid-flight to demonstrate control authority in both directions. (Bottom) Yaw angle (degree) response in a flight in which the set-point is changed mid-flight. The robot reacts quickly to the change in the set-point while hovering and approaches the set-point with small steady state error.

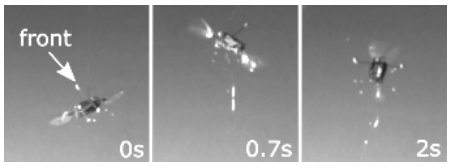

Fig. 16. Frames from a video in which the robot approaches and follows a trajectory of heading. Intermittent frame shows the heading close to the set-point of 60°, and the final frame shows the heading close to 0. These angles are measured about the Z-axis of the global coordinate frame.

flights (flight time of 1 second) demonstrating control authority in both directions.

C. Trajectory following

In Fig. 15 (bottom) it can be seen that the robot heading approached the desired set-point of +60° for first one second of the flight and zero heading for the next one second of the flight. During the flight, the robot could be seen steadying around the desired set-point before given the next set-point. The RMS error for the second set-point, calculated for last 0.5 sec is 0.33 rad. Frames from this flight are shown in Fig. 16. In the first frame, the robot heading before the take-off can be seen at $\sim 120°$. In the middle frame, which was captured at 0.7s, the robot heading was controlled to be at around $60°$. In the last frame, the robot was controlled to hover with zero heading. It can be seen in the videos that there is some coupling between altitude, lateral position, and absolute yaw angle; however, it is enough less than the previous designs that can fly. Additionally, the feedback controller makes sure to correct for any lateral drift and altitude changes while controlling the heading in flight.

VI. Conclusion

We have proposed and demonstrated experimentally three innovations by which to increase the yaw (z-axis) torque on flapping wing vehicles with a passive spring-like wing hinge. Our interest in such hinges is driven by their potential to be quieter less prone to failure than hinges with physical hinge angle limits [22]. The innovations are 1) a new robot fly design that increases the distance between the center of mass of the

robot and the center of pressure of the wings to increase the yaw torque moment arm, 2) wider actuators that increase the operating frequency, and 3) demonstration that the addition of a phase shift in the second harmonic signal can further increase yaw torque when driven off-resonance. We validated the results through simulation and robotic demonstration, showing for the first time, that it is possible to control yaw angle on such a vehicle while in controlled flight. This overcomes a significant limitation of previous two-actuator robot designs with spring wing hinges, which have been unable to actuate their yaw angle in controlled hovering flight [1], [2]. Experimental results were performed on a new design of an insect-sized aerial robot, called Robofly-expanded, weighing 160 mg. The robot design consists of two piezoelectric actuators and two wings to keep its design simple. Yaw torques were induced by adding a second harmonic signal to the fundamental frequency, resulting in differential drags in downstroke and upstroke. Our results build on [14] and [15], which revealed that the problem is more complicated than simply speeding up the upstroke relative to the downstroke.

As mentioned in the section on experimental results, the yaw command used for controlling the robot's heading was the second harmonic term, μ', in the voltage signals supplied to the actuators. Future work will experimentally confirm whether, in free flight, incorporating of phase shift in the second harmonic described in Section III can further increase yaw torque production.

The approach described here has the advantage of simplicity (two actuators vs. four) relative to the only other insect-sized system we are aware of that has achieved controlled yaw while hovering [10]. In the latter work, two additional piezoelectric actuators and a mechanism were incorporated to adjust the neutral angle of the wing hinge. Controlled yaw in controlled flight with a fully passive spring-like hinge has not previously been demonstrated, indicating the difficulty of the challenge. Actuation entails changes in wing kinematics that often affect other degrees of freedom, complicating flight control.

Our results indicate that yaw torque is complex phenomenon and highly dependent on parameter values that are either hard to measure or prone to change. For example, wing inertia can change with the addition of a small amount of glue during repair. Circumstantial observations from our simulation suggest that when the system is driven at the resonant frequency, a phase shift does not improve yaw torque, which merits further investigation. Known effects of flapping-wing flight [23] were not incorporated into the present model for simplicity, including viscosity, added mass, and the Kramer effect. Therefore, there may be additional mechanisms to actuate yaw that have not yet been explored. In practice, we propose that a phase tuning operation be added to the vehicle trimming process to maximize yaw torque [5].

ACKNOWLEDGEMENTS

Authors would like to thank Johannes James and Vikram Iyer for insightful discussion. Authors also appreciate Hari Krishna Hari Prasad's help during fabrication. This work was partially supported by the Air Force Office of Scientific Research under grant no. FA9550-14-1-0398.

REFERENCES

[1] K. Y. Ma, P. Chirarattananon, S. B. Fuller, and R. J. Wood, "Controlled flight of a biologically inspired, insect-scale robot," *Science*, vol. 340, no. 6132, pp. 603–607, 2013.

[2] Y. M. Chukewad, A. T. Singh, J. M. James, and S. B. Fuller, "A new robot fly design that is easier to fabricate and capable of flight and ground locomotion," in *2018 IEEE/RSJ International Conference on Intelligent Robots and Systems (IROS)*. IEEE, 2018, pp. 4875–4882.

[3] Y. M. Chukewad, J. James, A. Singh, and S. Fuller, "Robofly: An insect-sized robot with simplified fabrication that is capable of flight, ground, and water surface locomotion," *arXiv preprint arXiv:2001.02320*, 2020.

[4] J. James, V. Iyer, Y. Chukewad, S. Gollakota, and S. B. Fuller, "Liftoff of a 190 mg laser-powered aerial vehicle: The lightest wireless robot to fly," in *2018 IEEE International Conference on Robotics and Automation (ICRA)*. IEEE, 2018, pp. 1–8.

[5] D. Dhingra, Y. M. Chukewad, and S. B. Fuller, "A device for rapid, automated trimming of insect-sized flying robots," *IEEE Robotics and Automation Letters*, vol. 5, no. 2, pp. 1373–1380, 2020.

[6] S. B. Fuller, J. P. Whitney, and R. J. Wood, "Rotating the heading angle of underactuated flapping-wing flyers by wriggle-steering," in *2015 IEEE/RSJ International Conference on Intelligent Robots and Systems (IROS)*. IEEE, 2015, pp. 1292–1299.

[7] K. Sum Wu, J. Nowak, and K. S. Breuer, "Scaling of the performance of insect-inspired passive-pitching flapping wings," *Journal of the Royal Society Interface*, vol. 16, no. 161, p. 20190609, 2019.

[8] K. Y. Ma, S. M. Felton, and R. J. Wood, "Design, fabrication, and modeling of the split actuator microrobotic bee," in *Intelligent Robots and Systems (IROS), 2012 IEEE/RSJ International Conference on*. IEEE, 2012, pp. 1133–1140.

[9] R. J. Wood, "The first takeoff of a biologically inspired at-scale robotic insect," *IEEE transactions on robotics*, vol. 24, no. 2, pp. 341–347, 2008.

[10] Z. E. Teoh, "Design of hybrid passive and active mechanisms for control of insect-scale flapping-wing robots," Ph.D. dissertation, 2015.

[11] Z. E. Teoh and R. J. Wood, "A bioinspired approach to torque control in an insect-sized flapping-wing robot," in *5th IEEE RAS/EMBS International Conference on Biomedical Robotics and Biomechatronics*. IEEE, 2014, pp. 911–917.

[12] Z. Teoh and R. Wood, "A flapping-wing microrobot with a differential angle-of-attack mechanism," in *2013 IEEE International Conference on Robotics and Automation*. IEEE, 2013, pp. 1381–1388.

[13] S. B. Fuller, "Four wings: An insect-sized aerial robot with steering ability and payload capacity for autonomy," *IEEE Robotics and Automation Letters*, vol. 4, no. 2, pp. 570–577, 2019.

[14] N. Gravish and R. J. Wood, "Anomalous yaw torque generation from passively pitching wings," in *2016 IEEE International Conference on Robotics and Automation (ICRA)*. IEEE, 2016, pp. 3282–3287.

[15] R. Steinmeyer, P. H. Nak-seung, E. F. Helbling, and R. J. Wood, "Yaw torque authority for a flapping-wing micro-aerial vehicle," in *2019 International Conference on Robotics and Automation (ICRA)*. IEEE, 2019, pp. 2481–2487.

[16] N. T. Jafferis, M. A. Graule, and R. J. Wood, "Non-linear resonance modeling and system design improvements for underactuated flapping-wing vehicles," in *2016 IEEE International Conference on Robotics and Automation (ICRA)*. IEEE, 2016, pp. 3234–3241.

[17] M. H. Dickinson, F.-O. Lehmann, and S. P. Sane, "Wing rotation and the aerodynamic basis of insect flight," *Science*, vol. 284, no. 5422, pp. 1954–1960, 1999.

[18] J. P. Whitney and R. J. Wood, "Aeromechanics of passive rotation in flapping flight," *Journal of fluid mechanics*, vol. 660, pp. 197–220, 2010.

[19] S. P. Sane and M. H. Dickinson, "The control of flight force by a flapping wing: lift and drag production," *Journal of experimental biology*, vol. 204, no. 15, pp. 2607–2626, 2001.

[20] S. Sane and M. H. Dickinson, "The aerodynamic effects of wing rotation and a revised quasi-steady model of flapping flight," *Journal of experimental biology*, vol. 205, no. 8, pp. 1087–1096, 2002.

[21] B. M. Finio, N. O. Pérez-Arancibia, and R. J. Wood, "System identification and linear time-invariant modeling of an insect-sized flapping-wing micro air vehicle," in *2011 IEEE/RSJ International Conference on Intelligent Robots and Systems*. IEEE, 2011, pp. 1107–1114.

[22] Z. Tu, F. Fei, J. Zhang, and X. Deng, "An at-scale tailless flapping-wing hummingbird robot. i. design, optimization, and experimental validation," *IEEE Transactions on Robotics*, 2020.

[23] S. P. Sane, "The aerodynamics of insect flight," *Journal of experimental biology*, vol. 206, no. 23, pp. 4191–4208, 2003.